A Study of 2D Roughness Periodical Profiles on a Flat Surface Generated by Milling with a Ball Nose End Mill

Mihaita Horodinca *, Florin Chifan, Emilian Paduraru, Catalin Gabriel Dumitras, Adriana Munteanu, Dragos-Florin Chitariu

Posted Date: 21 February 2024

doi: 10.20944/preprints202402.1238.v1

Keywords: 2D roughness profiles; milling; ball nose end mill, curve (signal) fitting, fast Fourier transform.

 doi:10.20944/preprints202402.1238.v1

Article

A Study of 2D Roughness Periodical Profiles on a Flat Surface Generated by Milling with a Ball Nose End Mill

Mihaita Horodinca *, Florin Chifan, Emilian Paduraru, Catalin-Gabriel Dumitras, Adriana Munteanu and Dragos Florin Chitariu

Digital Manufacturing Systems Department, "Gheorghe Asachi" Technical University of Iasi, 700050 Iasi, Romania; florin.chifan@academic.tuiasi.ro (F.C.); emilian.paduraru@academic.tuiasi.ro (E.P.); catalin-gabriel.dumitras@academic.tuiasi.ro (C.-G.D.); adriana.munteanu@academic.tuiasi.ro (A.M.); dragos-florin.chitariu@academic.tuiasi.ro (D-F.C.)

* Correspondence: mihaita.horodinca@academic.tuiasi.ro; Tel.: +0040742577846

Abstract: This paper presents a study of the 2D roughness profiles on a flat surface generated on a steel work piece, by ball nose end milling, with linear equidistant tool paths (pick-intervals). The milled surface exploration with a surface roughness tester (on pick and feed directions) produces usually 2D roughness profiles having periodical evolutions. These evolutions can be seen as time-dependent signals, describable as a sum of sinusoidal components (the wavelength of each component being regarded as a period). In order to detect a well approximated description of these components, two appropriate signal processing techniques are used in this work: first technique provides a direct mathematical (analytical) description and is based on computer aided curve (signal) fitting (more accurate), the second technique (providing an indirect and incomplete description) is based on the spectrum generated by fast Fourier transform (less accurate). This study can be seen as a way for a better understanding the interaction between the tool and the work piece or to achieve a mathematical description of the machined surface microgeometry in terms of roughness (e. g. its description being a collection of closely spaced 2D roughness profiles).

Keywords: 2D roughness profiles; milling; ball nose end mill; curve (signal) fitting; fast Fourier transform

1. Introduction

The surface roughness of machined steel work pieces by milling with ball nose end mills is obviously strictly related with the interaction between tool and work piece. Mainly it depends by cutting tool shape, geometry and position (tilt angle, axial depth of cut, effective cutting diameter), cutting machining parameters (cutting speed, feed rate and direction) milling strategy (tool path patterns, step over distance) and cutting forces (involved in tool elastic deformations). Some non-systematic phenomena are occasionally also involved in the definition of this roughness: tool work piece relative vibrations, self-excited vibrations, local variation of hardness on work piece material, tool wear, cutting edge adhesions or fractures, etc. Therefore, in the most appropriate milling conditions, the roughness is mainly characterized by a microgeometry with a regular (periodical) shape with equidistant pick (path)-interval and feed-interval scallops [1] on pick and feed directions.

A better understanding of tool-work piece interaction during any cutting process supposes a deep investigation of the surfaces roughness. First approach in this investigation is the experimental sampling of surfaces roughness description using appropriate equipment. The most common method to achieve this sampling is to use contact profilometers [2-8] as reliable but time-consuming method. Some other methods use the non-contact surface exploration by lasers [9], laser interferometry [10, 11], laser confocal microscopes [12], optical systems [13, 14] or machine vision systems [15].

Because generally the description of a 3D surface roughness by sampling is obtained by joining many 2D roughness profiles (e. g. as a grid on pick and feed directions), the investigation of these

 doi:10.20944/preprints202402.1238.v1

surfaces means mainly a study on each of these 2D roughness profiles (2DRPs), frequently as having a periodic evolution [2, 4, 5, 8, 9, 13, 14 and 16]. Some investigation techniques on this topic are available in literature, most of these revealing the existence of numerous permanent sinusoidal components inside these 2DRPs (as wavinesses [16], with dominants and some harmonics). Some previous studies indicate the availability of component finding description techniques using synthetic rather than analytic methods, the 2DRPs being treated mainly as digital time-dependent signals. The easiest synthetic description of components can be obtained by digital filtering [17], particularly using a selective band pass filtering [8]. A relative better approach in this synthetic description is possible using the power spectral density (by fast Fourier transform, FFT) of 2DRPs as signals [2, 7, 8, 15 and 16]. On a FFT spectrum (with amplitude on y-axis and conventional frequency as the inverse of the wavelength on x-axis) each significant sinusoidal component inside a 2DRP is described as a peak. However, the availability of FFT is seriously affected generally by a small resolution of conventional frequency (R_{cf}) on spectra. The using of a high sampling rate (or sampling frequency f_s as well) for 2DRP description (in order to have a high Nyquist limit $f_{Nq} = f_s/2$) should be mandatory accompanied by a high number (N) of samples (or a big size, length, of 2DRP) in order to have a small resolution of conventional frequency $R_{cf} = f_s/N$. If this resolution is not small enough, some peaks in spectrum are missing or have wrong described amplitude (smaller than normal). This is a major inconvenient of FFT, not yet resolved in these previous approaches. However, there is a supplementary inconvenient of analysis by FFT: the synthetic description of sinusoidal components is incomplete (their phases at the origin of time are missing).

In some cases the 2DRPs, seen as time-dependent signals, contains short sinusoidal components which don't persist permanently. For these situations (not considered in our work), when generally short oscillations (waves) occurs temporarily, the FFT analysis is not at all appropriate, but there are available other specific investigation techniques (inspired by the study of vibrations), e. g. based on Wavelet Transform (as Continuous Wavelet Transform [7], Frequency Normalized Wavelet Transform [18, 19] and Wavelet Packet Transform [20]).

The main purpose of this work is focused on the investigation of periodical 2DRPs (seen as time-dependent signals) in order to find out the best analytical approximation of them, as close as possible to experimental evolutions, as a sum of significant sinusoidal components. Each sinusoidal component (analytically defined by the amplitude, a conventional frequency and a phase at the conventional origin of time) is a description of a waviness on the machined surface of work piece. The inverse of the conventional frequency (as conventional period) is the waviness wavelength.

Particularly, these 2DRPs are experimentally sampled in feed and pick directions (using a contact profilometer) on a theoretically flat surface milled with a ball nose end mill. A curve fitting procedure in Matlab (based on *Curve fitting Toolbox*) will be privileged in this approach. As opposed to the FFT procedure (also addressed here), now even relative small size (length) 2DRPs are appropriate for curve fitting procedure, high accuracy in analytical description of sinusoidal components being attainable. Similarly with FFT procedure, the curve fitting procedure has the same Nyquist limit ($f_{Nq} = f_s/2$), in other words it is not possible to find out the analytical descriptions of sinusoidal components having conventional frequency above the Nyquist limit f_{Nq}. The curve fitting procedure allows an interesting approach: a 2DRP in analytical description can be artificially resized by mathematical extrapolation (increasing the number N of samples, keeping the same sampling rate f_s). The accuracy of the FFT spectrum of this resized 2DRP is significantly improved due a smaller conventional frequency resolution, so now the FFT spectrum is more appropriate to describe synthetically the contents (in sinusoidal components) of a 2DRP.

The next sections of this paper are organized as it follows: Section 2 presents the materials and methods, Section 3 presents the results and discussions and Section 4 presents the conclusions.

2. Materials and Methods

A flat surface was milled on a work piece made by 90MnCrV8 steel (60 HRC hardness) using a carbide 12 mm 3 flute ball nose end mill, TiAlN coated (as GARANT Diabolo solid carbide ball nose slot drill HPC 12 mm, from Hoffmann Group), tilted with 25 degrees to the pick direction and

 doi:10.20944/preprints202402.1238.v1

perpendicular to the feed direction, with these cutting regime parameters: 5200 rpm, 1560 mm/min feed rate, constant 0.1 mm axial depth of cutting and 0.4 mm step over (with theoretical equals pick-interval scallops height [21]). Figure 1 presents a down milling process conceptual description (with the work piece in cyan color, the tool in red, the feed direction in green, the rotation sense in blue). The magenta colored straight line (d1) depicts the pick direction; the black colored line (d2) depicts the feed direction, both used conventionally for experimentally sampling of 2DRP (with a SURFTEST SV-2100W4 contact profilometer, from Mitutoyo). Figure 2 presents a view of tool and work piece (with the cutting process stopped) on a vertical machining center CNC OKUMA GENOS M460R-VE.

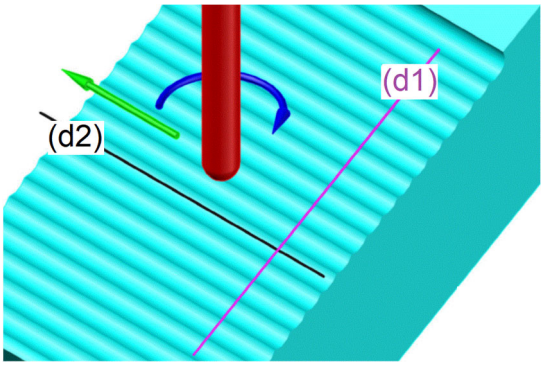

Figure 1. A conceptual description of cutting process.

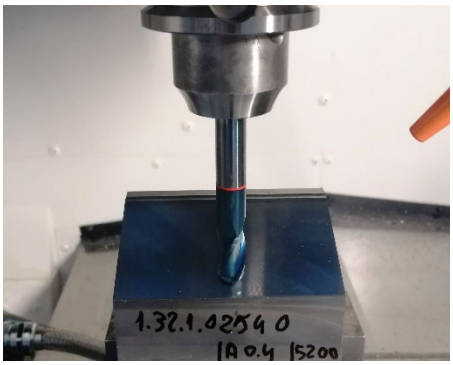

Figure 2. A view on milling setup.

Figure 3 presents a view on the roughness sampling setup, with the flat milled surface placed in horizontal position (here for sampling in pick direction).

Figure 3. A view on the roughness sampling setup.

The numerical description of a 2DRP is delivered as a two-column .txt files describing 8,000 equidistant samples ($\Delta x = 0.5\ \mu m$ sampling interval between samples on x-axis, for 4 mm total

 doi:10.20944/preprints202402.1238.v1

distance). This file is easy loadable in Matlab and analyzable as time-depending signal (by FFT and curve (signal) fitting). Figure 4 presents a 4 mm length 2DRP, sampled in pick direction (drawn in Matlab). As expected, there is a dominant periodical component inside. A rough estimation on Figure 4 indicates 10 periods, each period being equal to the milling step over (400 micrometers) and an average pick-interval scallop height of 2.5 micrometers.

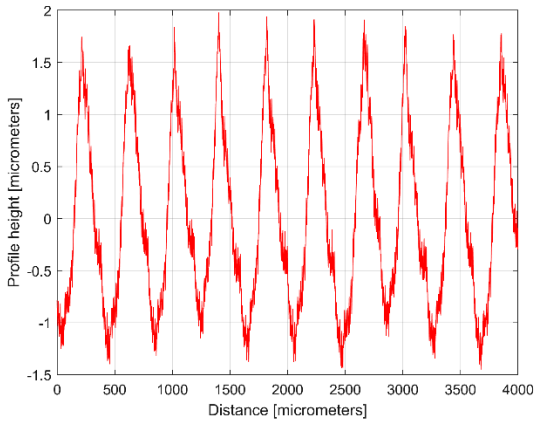

Figure 4. Graphical description of a 2DRP sampled on work piece, in pick direction.

Figure 5 presents a partial view of the FFT spectrum of this 2DRP with real amplitudes (in Matlab). The 2DRP from Figure 4 was processed in FFT as a time-dependent signal (the x-coordinates of samples are seen as signal samples time; the y-coordinates are seen as signal level). The sampling interval Δx on x-axis ($\Delta x=0.5\ \mu m$) is seen as conventional sampling period Δt on t-axis. An x-coordinate on the abscissa of Figure 5 is the equivalent of a conventional frequency or the inverse of a conventional period or an inverse of a wavelength as well. A peak on FFT spectrum (e. g. the highest peak , depicted by an x-coordinate of 0.0025 μm^{-1} and a y-coordinate of 1.138 μm) indicates that in the 2DRP exists a dominant sinusoidal component having the wavelength $\lambda=1/x$ (e. g. $\lambda_1 = 1/0.0025 = 400\ \mu m$ for the peak 1). This is exactly the step over value (pick feed) previously highlighted. On Figure 5 some other relevant peaks (2, 3, 4 and 5) depict sinusoidal components, harmonically correlated with the dominant, the i^{th} harmonic (with i =1, 2, 3 and 4) having the wavelengths $\lambda_i = \lambda_1/(i+2)$ as 200, 133.(3), 100 and 80 μm. The conventional sampling period $\Delta t = 0.5\mu m$ depicts the sampling frequency (rate) $f_s = 1/\Delta t = 2\ \mu m^{-1}$ so a conventional Nyquist limit (frequency) of $f_{Nq} = f_s/2 = 1\mu m^{-1}$. In other words, the smaller synthetic describable wavelength of a sinusoidal component inside the 2DRP by FFT spectrum is defined as $\lambda_{min} = (f_{Nq})^{-1} = (f_s/2)^{-1} = 1\ \mu m$.

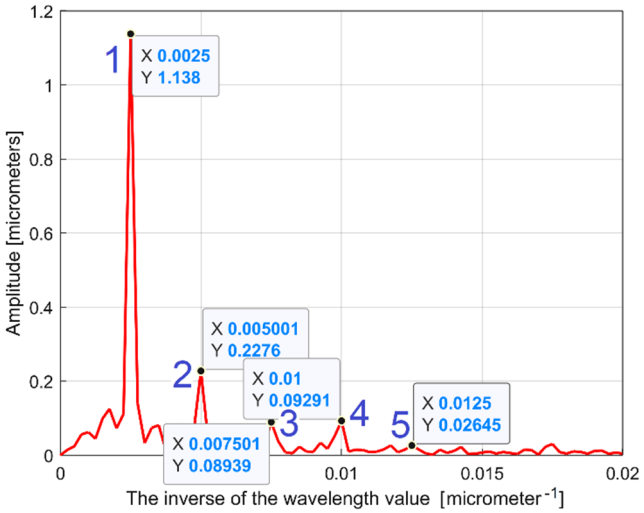

Figure 5. A partial view on the FFT spectrum of 2DRP from Figure 4.

 doi:10.20944/preprints202402.1238.v1

However, as it is clear indicated on Figure 5, the conventional frequency resolution $R_{cf} = f_s/N = 2/8000 = 0.00025\ \mu m^{-1}$ is not small enough in order to describe an accurate spectrum. On the spectrum from Figure 5 there are only $0.02/R_{cf} = 0.02/0.00025 = 80$ samples. There are certainly other higher harmonics that are not visible in spectrum. A longer 2DRP (obtained by increasing the number of samples and keeping the same sampling frequency) reduces significantly the conventional resolution. It must be stated again that the FFT spectrum doesn't provide the phase at origin of conventional time ($x=0$) for sinusoidal components.

A better approach proposed in this paper considers that inside the $y(x)$ 2DRP is a consistent deterministic part $y_d(x)$ and a less significant non deterministic part $y_{nd}(x)$, with $y(x) = y_d(x) + y_{nd}(x)$. Generally, for periodical 2DRPs, this deterministic part $y_d(x)$ is describable as a sum of n sinusoidal components:

$$y_d(x) = \sum_{j=1}^{n} y_{dj}(x) = \sum_{j=1}^{n} A_j \cdot \sin(\omega_j \cdot x + \varphi_j) \qquad (1)$$

In Eq. (1) A_j are amplitudes, ω_j are conventional angular frequencies (related by wavelengths λ_j, with $\omega_j = 2\pi/\lambda_j$) and φ_j are conventional phase shifts at origin ($x = 0$). Here x (the current position of the profilometer stylus on x- axis) plays the role of time.

The curve (signal) fitting procedure (using *Curve fitting tool* from Matlab) allows finding out with a good approximation the coefficients A_j, ω_j and φ_j. A sine model (f(x)=a1*sin(b1*x+c1) was used for a first fitting with x as X data and y as Y data. In this model a1, b1 and c1 plays the role of A_1, ω_1 and φ_1 coefficients in definition of first sinusoidal component $y_{d1}(x)$. The first curve fitting produces the results $A_1 = 1.151\ \mu m$, $\omega_1 = 0.01558\ rad/\mu m$ and $\varphi_1 = 4.1871\ rad$ (usually this fitting procedure find the description of the highest amplitude component). This first sinusoidal component $y_{d1}(x)$ is depicted in blue color on Figure 6 (as dominant), overlaid on $y(x)$, depicted in red color (an evolution already described in Figure 4). Thus the component $y_{d1}(x)$ can be mathematically described as:

$$y_{d1}(x) = A_1 \cdot \sin(\omega_j \cdot x + \varphi_j) = 1.151 \cdot \sin(0.01557 \cdot x + 4.1871) \qquad (2)$$

The description of $y_{d1}(x)$ from Eq. (1) allows the mathematical removing from $y(x)$, with the result depicted in Figure 7, as the first residual ($r_1(x)$) 2DRP, $r_1(x) = y(x) - y_{d1}(x)$ after first curve fitting (drawn at the same scale with Figure 6). The decrease of y-coordinates of the residual profile is a supplementary proof of the quality of $y_{d1}(x)$ mathematical description.

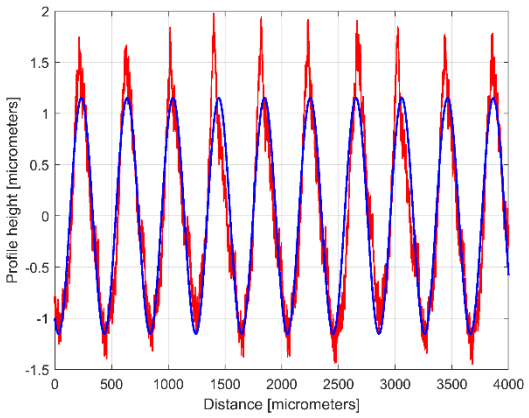

Figure 6. The 2DRP from Figure 4 (in red) and the first sinusoidal component ($y_{d1}(x)$) found by curve (signal) fitting (in blue), Eq. (2).

Preprints.org (www.preprints.org) | NOT PEER-REVIEWED | Posted: 21 February 2024 doi:10.20944/preprints202402.1238.v1

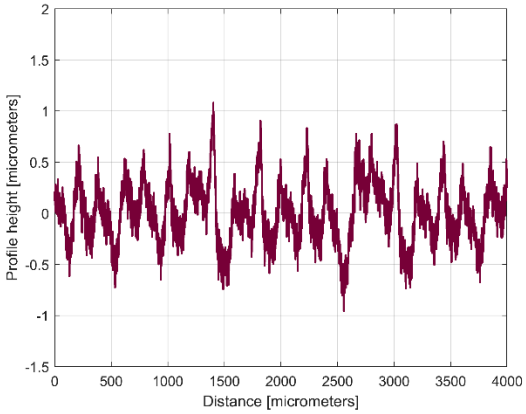

Figure 7. The first residual 2DRP after first analysis by curve fitting (as $r_1(x) = y(x)-y_{d1}(x)$).

It is obvious that the dominant component $y_{d1}(x)$ really fits with $y(x)$. Its amplitude A_1 is close by this depicted in FFT spectrum (peak 1), its wavelength $\lambda_1 = 2\pi/\omega_1 = 2\pi/0.01558 = 403.285\ \mu m$, is close by the step over value or pick feed ($400\ \mu m$) during the milling process. The conventional frequency of $y_{d1}(x)$ is $1/\lambda_1 = 0.002479\ \mu m^{-1}$, more accurately described by comparison with Figure 5, related to the first peak (there $1/\lambda_1 = 0.0025\ \mu m$). Related by the difference between $\lambda_1 = 403.285\ \mu m$ (determined by curve fitting) and the pick feed ($400\ \mu m$), a logical conclusion must be drawn: we rather suspect the imprecise control of the x-movement of the contact profilometer during measurement than the pick feed control during milling process.

It is clear that this procedure can be repeated identically (automatically, by programming in Matlab) many times, the mathematical description of the $y_{dj}(x)$ sinusoidal component can be found by curve fitting of the $(j-1)^{th}$ residual of 2DRP, as $r_{j-1}(x)$, described with:

$$r_{j-1}(x) = y(x) - \sum_{k=1}^{j-1} y_{dk}(x) \qquad (3)$$

Of course, in curve fitting procedure (as in the case of the FFT spectrum) the exceeding of the Nyquist limit is forbidden ($\omega_j < 2\pi f_{Nq}$ or $\lambda_j > (f_{Nq})^{-1}$).

Hypothetically, considering that $y_{nd}(x) = 0$, a perfect mathematically description of $y_d(x)$ (after n curve fitting similar steps), should produce an $r_n(x) = 0$ for the n^{th} residual of 2DRP (graphically representable as a straight line placed on the x-axis).

The viability of this method of determining the mathematical description of a roughness profile (by a similar curve fitting method developed in Matlab) has been demonstrated before [22] in the analysis of other types of complex signals (vibrations, active electrical power, instantaneous angular speed, etc.) containing many sinusoidal components.

3. Results and Discussions

3.1. The Analysis of 2D Roughness Profiles in Pick Direction by Curve Fitting

The analysis of the 2DRP already sampled before (Figure 4) has been done similarly by this curve fitting procedure another 121 times. The mathematical description of 122 sinusoidal components inside $y(x)$ was found. Figure 8 presents the 2DRP (already depicted in red color on Figures 4 and 6) overlaid on an approximation of $y_d(x)$ by mathematical addition of these 122 sinusoidal components (in blue color). On the same Figure is overlaid the 122^{th} residual of 2DRP ($r_{122}(x)$), depicted in purple color. Figure 9 presents a zoom-in detail in area A from Figure 8.

Preprints.org (www.preprints.org) | NOT PEER-REVIEWED | Posted: 21 February 2024 doi:10.20944/preprints202402.1238.v1

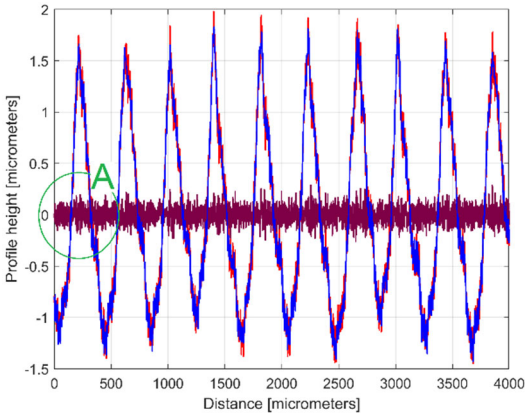

Figure 8. The 2DRP (in red), an approximation of $y_d(x)$ with $y_{dh}(x)$ having 122 components (in blue) and the 122th residual $r_{122}(x)$, (in purple).

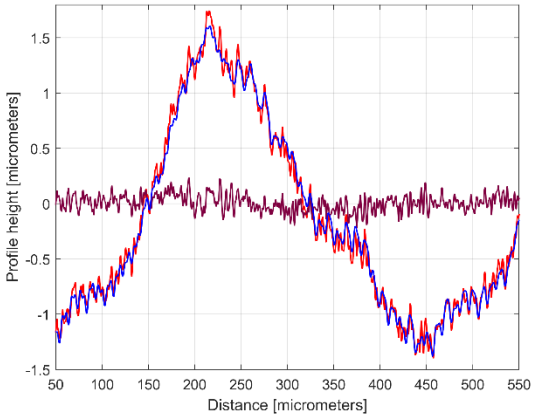

Figure 9. A zoom-in detail in area A from Figure 8.

It is obvious that there is a good fit between the approximation of $y_d(x)$ and $y(x)$. By comparison with Figure 7 there is a significant smaller residual of 2DRP, mainly describing the nondeterministic content $y_{nd}(x)$ of $y(x)$.

As is well known [23], any evolution of a signal in time (or similar, e. g. this 2DRP in pick direction) can be well approximated as a sum of sinusoidal components. In our approach it is more interesting to find its approximated analytical description (strictly related by milling process) as a sum of harmonically correlated sinusoidal components (as $y_{dh}(x)$) with a fundamental on 0.01557 rad/μm as conventional angular frequency ω_1 (Eq. (2)) related by pick feed or step over and some harmonics (on $2 \cdot 0.01557$ *rad/μm*, $3 \cdot 0.01557$ *rad/μm* frequency, so on). In other words, the deterministic part of $y(x)$ should be seen as $y_d(x) = y_{dh}(x) + y_{dnh}(x)$, with $y_{dnh}(x)$ as a sum of sinusoidal non-harmonically correlated components. Of course, this new type of approximation is available here because $y_{dh}(x)$ is dominant ($y_d(x) \approx y_{dh}(x)$).

Among the 122 identified sinusoidal components, 30 components were found to be well harmonically correlated (and involved in $y_{dh}(x)$ definition from Eq. (4)) with a good approximation, with the values A_{Hi}, ω_{Hi} and φ_{Hi} given in Table 1.

$$y_{dh}(x) = \sum_{i=1}^{30} A_{Hi} \cdot \sin(\omega_{Hi} \cdot x + \varphi_{Hi}) \qquad (4)$$

 doi:10.20944/preprints202402.1238.v1

Table 1. The values of constants involved in the mathematical description of 30 well harmonically correlated sinusoidal components inside ydh(x) of the 2DRP, in pick direction.

Harmonic # (*Hi*)	Amplitude A_{Hi} [μm]	Conventional angular frequency ω_{Hi} [rad/μm]	Wavelength $\lambda_{Hi}=2\pi/\omega_i$ [μm]	Phase φ_{Hi} at origin ($x=0$) [rad]
H1	A_{H1}=1.148	ω_{H1}=0.01557	λ_{H1}=403.544	φ_{H1} =4.2031
H2	0.2459	0.03118 (as 2.0025· ω_{H1})	201.53 (as λ_{H1}/2.0024)	1.412
H3	0.09367	0.04669 (as 2.9987· ω_{H1})	134.57 (as λ_{H1}/2.9988)	4.3261
H4	0.1116	0.06239 (as 4.0070· ω_{H1})	100.70 (as λ_{H1}/4.0074)	2.456
H5	0.02461	0.07848 (as 5.0404· ω_{H1})	80.061 (as λ_{H1}/5.0405)	3.085
H7	0.03816	0.1092 (as 7.0138· ω_{H1})	57.538 (as λ_{H1}/7.0135)	4.785
H8	0.009202	0.1245 (as 7.9961· ω_{H1})	50.467 (as λ_{H1}/7.9962)	5.8120
H9	0.0236	0.1404 (as 9.0173· ω_{H1})	44.752 (as λ_{H1}/9.0173)	3.4731
H10	0.02267	0.1558 (as 10.0064· ω_{H1})	40.328 (as λ_{H1}/10.0065)	4.6591
H11	0.0129	0.1714 (as 11.0083· ω_{H1})	36.658 (as λ_{H1}/11.0083)	1.21
H12	0.01171	0.1873 (as 12.0295· ω_{H1})	33.546 (as λ_{H1}/12.0296)	5.3275
H13	0.01317	0.2027 (as 13.0186· ω_{H1})	30.997 (as λ_{H1}/13.0188)	1.796
H14	0.01174	0.2181 (as 14.0077· ω_{H1})	28.808 (as λ_{H1}/14.0081)	5.8364
H15	0.01097	0.2337 (as 15.0096· ω_{H1})	26.885 as λ_{H1}/15.0100)	5.3481
H16	0.01386	0.2493 (as 16.0016· ω_{H1})	25.203 (as λ_{H1}/16.0117)	3.097
H18	0.01152	0.2805 (as 18.0154· ω_{H1})	22.399 (as λ_1/18.0162)	5.5279
H19	0.0192	0.2961 (as 19.0173· ω_{H1})	21.219 (as λ_{H1}/19.0180)	0.628
H22	0.01029	0.3425 (as 21.9974· ω_{H1})	18.345 (as λ_{H1}/21.9975)	3.9651
H23	0.008842	0.3586 (as 23.0315· ω_{H1})	17.521 (as λ_{H1}/23.0320)	2.8171
H24	0.02065	0.3741 (as 24.0270· ω_{H1})	16.795 (as λ_{H1}/24.0276)	4.3321
H25	0.009471	0.3896 (as 25.0225· ω_{H1})	16.127 (as λ_{H1}/25.0229)	1.299
H26	0.01693	0.4053 (as 26.0308· ω_{H1})	15.502 (as λ_{H1}/26.0317)	1.822
H27	0.01081	0.4208 (as 27.0263· ω_{H1})	14.931 (as λ_{H1}/27.0273)	4.2351
H28	0.009238	0.4365 (as 28.0347· ω_{H1})	14.394 (as λ_{H1}/28.0356)	1.563
H29	0.007853	0.4524 (as 29.0559· ω_{H1})	13.888 (as λ_{H1}/29.0570)	0.7781
H31	0.01326	0.4833 (as 31.0405· ω_{H1})	13.000 (as λ_{H1}/31.0418)	0.5155
H32	0.01014	0.4985 (as 32.0167· ω_{H1}	12.604 (as λ_{H1}/32.0171)	3.9471
H38	0.008485	0.5924 (as 38.0475· ω_{H1})	10.606 (as λ_{H1}/38.0487)	5.7423
H41	0.02497	0.6392 (as 41.0533· ω_{H1})	9.829 (as λ_{H1}/41.0565)	1.478
H42	0.01782	0.6548 (as 42.0552· ω_{H1})	9.595 (as λ_{H1}/42.0577)	0.9996

Some harmonics are missing (e. g. H6, H17, H20, H21, etc.).

Figure 10 presents an equivalent of Figure 8 but with an approximation of $y_d(x)$ with $y_{dh}(x)$ according with Eq. (4) and Table 1. Figure 11 presents a zoom in detail in area A on Figure 10 (similarly with Figure 9).

A comparison of Figures 10 and 11 with Figures 8 and 9 proves that the fitting is acceptable but less good as before, aspect well highlighted by the evolution of the residual ($r_{30}(x)$). Especially in some areas (e. g. B, C and D on Figure 10) the fit between $y(x)$ and $y_{dh}(x)$ is locally less good. There are some reasons for this misfit. Firstly, we should consider the angular position of the milling tool (due to its rotation). This position was not rigorously the same each time when its axis intersects the line (e. g.

Preprints.org (www.preprints.org) | NOT PEER-REVIEWED | Posted: 21 February 2024 doi:10.20944/preprints202402.1238.v1

(d1) on Figure 1) where the 2DRP was sampled (the pick-interval scallops geometry on this line from working piece is slightly different). Secondly, there are variable flexional deformation of the milling tool on the direction of this line (on pick feed direction).

However, in this approach, the $y_{dh}(x)$ evolution (depicted separately in Figure 12) provides one of the best characterizations of the 2DRP, systematically related by the interaction between milling tool and work piece.

Due to a small imprecision of curve (signal) fitting process, there is not a perfect harmonic correlation between the 30 components inside $y_{dh}(x)$, as it is clear indicated on Table 1 (with $\omega_{Hi} \approx H_i \cdot \omega_{H1}$ or $\lambda_{Hi} \approx \lambda_{H1}/H_i$ as well), the $y_{dh}(x)$ evolution from Figure 12 is not strictly periodical, as expected.

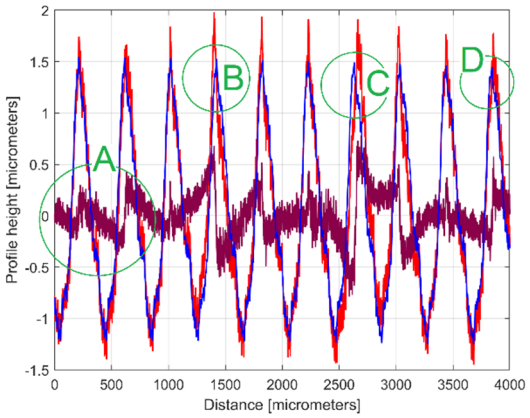

Figure 10. The 2DRP (in red), an approximation of $y_d(x)$ with a $y_{dh}(x)$ profile having 30 components described in Table 1 (in blue) and the 30th residual $r_{30}(x)$ (in purple).

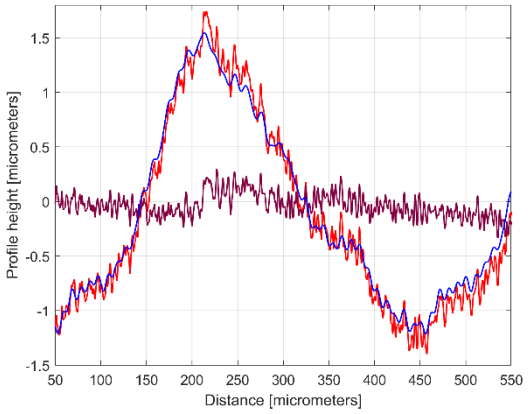

Figure 11. A zoom-in detail in area A from Figure 10.

This inconvenient can be simply avoided, roughly considering in Eq. (4) $\omega_{Hi} = H_i \cdot \omega_{H1}$. A rigorously approach, is the replacing in $\omega_{Hi} = H_i \cdot \omega_{H1}$ the conventional angular frequency ω_{H1} with a more probable equivalent value ω_{He1}, calculated as:

$$\omega_{He1} = \left(\sum_{i=1}^{30} \frac{A_{Hi}}{A_{H1}}\right)^{-1} \cdot \sum_{i=1}^{30} \frac{A_{Hi}}{A_{H1}} \frac{\omega_{Hi}}{H_i} = 0.0155785 \text{ rad/}\mu\text{m} \qquad (5)$$

In ω_{He1} the weighting (by amplitude A_{Hi}) of conventional angular frequency ω_{Hi} of each harmonic, relative to the amplitude A_{H1} of the first harmonic H1 (as dominant) is considered. However there is no significant difference between ω_{H1} and ω_{He1}.

With this value ω_{He1} the description of $y_{dh}(x)$ from Eq. (4) can be rewritten as $y_{dhe}(x)$ according to Eq. (6) and graphically depicted according to Figure 13.

Preprints.org (www.preprints.org) | NOT PEER-REVIEWED | Posted: 21 February 2024 doi:10.20944/preprints202402.1238.v1

$$y_{dhe}(x) = \sum_{i=1}^{30} A_{Hi} \cdot \sin(H_i \cdot \omega_{He1} \cdot x + \varphi_{Hi}) \quad (6)$$

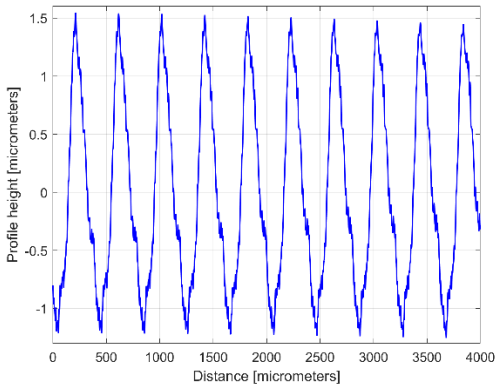

Figure 12. The evolution of $y_{dh}(x)$ profile.

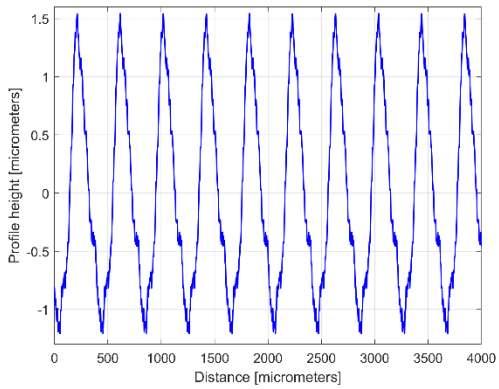

Figure 13. The evolution of $y_{dhe}(x)$ profile.

This $y_{dhe}(x)$ profile can be accepted as a systematic characterization (pattern) of the 2DRP in pick direction. Even a more interesting characterization is done if this $y_{dhe}(x)$ profile is described considering that the origin on x-axis ($x= 0$) is artificially moved in the abscissa $(2\pi\text{-}\varphi_{H1})/\omega_{He1}$ of the first zero-crossing point (from negative to positive values) of the dominant sinusoidal component (H1 in Table 1). Now $y_{dhe}(x)$ profile becomes $y_{dhe0}(x)$, mathematically described with Eq. (7) and graphically depicted in blue color on Figure 14. There the curve depicted with magenta color describes the dominant component (H1), moved in new origin (as $H1_0$), with ω_{H1} replaced with ω_{He1}.

$$y_{dhe0}(x) = \sum_{i=1}^{30} A_{Hi} \cdot \sin[H_i \cdot \omega_{He1} \cdot (x + \frac{2\pi - \varphi_{H1}}{\omega_{He1}}) + \varphi_{Hi}] \quad (7)$$

With Eq. (7) rewritten as Eq. (8), this move in a new origin is an equivalent of a positive shift of phase ($H_i \cdot (2\pi\text{-}\varphi_{H1})$) at origin for all the components:

$$y_{dhe0}(x) = \sum_{i=1}^{30} A_{Hi} \cdot \sin[H_i \cdot \omega_{He1} \cdot x + \varphi_{Hi} + H_i \cdot (2\pi - \varphi_{H1}))] \quad (8)$$

Figure 15 presents a zoom in detail of Figure 14, with a first period of $y_{dhe0}(x)$ profile and the component $H1_0$.

Preprints.org (www.preprints.org) | NOT PEER-REVIEWED | Posted: 21 February 2024 doi:10.20944/preprints202402.1238.v1

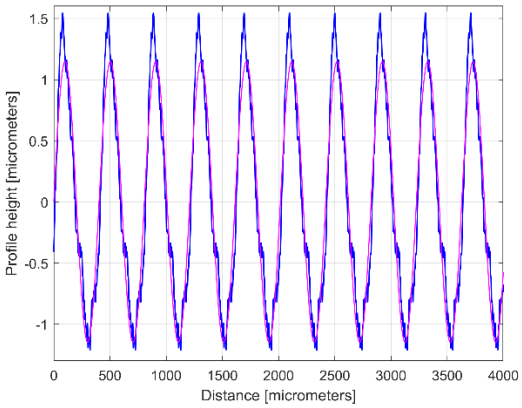

Figure 14. The evolution of $y_{dhe0}(x)$ profile (in blue) overlaid on the evolution of the dominant component $H1_0$ (in magenta).

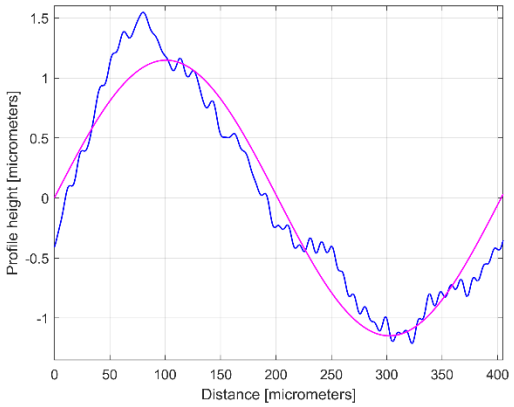

Figure 15. A zoom in detail of Figure 14 with first period of $y_{dhe0}(x)$ profile.

This $y_{dhe0}(x)$ type of 2DRP is useful when two (or more) 2DRPs sampled in similar condition are compared. In this approach, a second 2DRP was sampled on the same flat milled surface on a straight line parallel with (d1) on pick direction, a randomly chosen distance between (several millimeters).

As an equivalent of Figure 10, Figure 16 presents this new 2DRP (as $y(x)$, in red) having the same number of samples (*8,000*) and sampling interval (Δx=*0.5 μm*), overlapped with the $y_{dh}(x)$ profile (in green) and the residual (in purple). This time only 12 harmonically related sinusoidal components inside $y_{dh}(x)$ were found (Table 2) among the 122 sinusoidal components in $y_d(x)$.

Table 2. The values of constants involved in the mathematical description of 12 well harmonically correlated sinusoidal components inside $y_{dh}(x)$ of the 2nd 2DRP, sampled in pick direction.

Harmonic # (*Hi*)	Amplitude A_{Hi} [μm]	Conventional angular frequency ω_{Hi} [rad/μm]	Wavelength $\lambda_{Hi}=2\pi/\omega_i$ [μm]	Phase φ_{Hi} at origin (x=*0*) [rad]
H1	A_{H1}=*1.124*	ω_{H1}=*0.01552*	λ_{H1}=*404.8444*	φ_{H1} =*0.4821*
H2	0.2406	0.03099 (as *1.9968*· ω_{H1})	202.7488 (as λ_{H1}/*1.9968*)	0.407
H3	0.08159	0.04671 (as *3.0097*· ω_{H1})	134.5148 (as λ_{H1}/*3.0097*)	5.2621
H4	0.1232	0.06224 (as *4.0103*·ω_{H1})	100.9509 (as λ_{H1}/*4.0103*)	6.1897
H5	0.0234	0.07745 (as *4.9903*· ω_{H1})	81.1257 (as λ_{H1}/*4.9903*)	4.9971
H6	0.008268	0.09263 (as *5.9604*· ω_{H1})	67.8310 (as λ_{H1}/*5.9684*)	0.205
H7	0.03793	0.1088 (as *70103*· ω_{H1})	57.7499 (as λ_{H1}/*7.0103*)	3.7771

Preprints.org (www.preprints.org) | NOT PEER-REVIEWED | Posted: 21 February 2024 doi:10.20944/preprints202402.1238.v1

H9	0.01861	0.1404 (as $9.0464 \cdot \omega_{H1}$)	44.7520 (as $\lambda_{H1}/9.0464$)	0.1429
H10	0.02616	0.1558 (as $10.0387 \cdot \omega_{H1}$)	40.3285 (as $\lambda_{H1}/10.0387$)	3.6981
H11	0.01256	0.1712 (as $11.0309 \cdot \omega_{H1}$)	36.7008 (as $\lambda_{H1}/11.0309$)	2.608
H13	0.01106	0.2026 (as $13.0541 \cdot \omega_{H1}$)	31.0128 (as $\lambda_{H1}/13.0541$)	2.05
H22	0.0107	0.3425 (as $22.0683 \cdot \omega_{H1}$)	18.3451 (as $\lambda_{H1}/22.0683$)	1.326

As an equivalent of Figure 14, Figure 17 presents the evolution of $y_{dhe0}(x)$ profile (in green) overlaid on the evolution of the dominant component $H1_0$ (in brown).

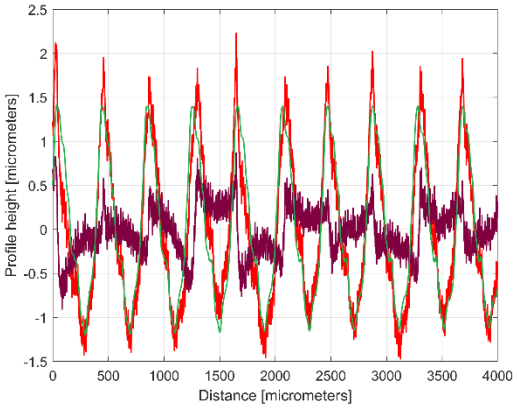

Figure 16. A new 2DRP (in red), an approximation of $y_d(x)$ with $y_{dh}(x)$ profile having 12 components (in green) and the 12th residual $r_{12}(x)$, (in purple). An equivalent of Figure 10.

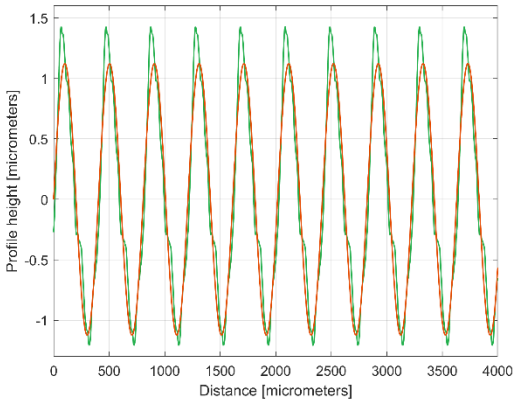

Figure 17. The evolution of $y_{dhe0}(x)$ profile (in green) overlaid on the evolution of the dominant component $H1_0$ (in brown). An equivalent of Figure 14.

It is interesting here to highlight the similarities (by comparison) between the $y_{dhe0}(x)$ profiles (from Figure 14 and 17), by their overlapping, on Figure 18. This is possible because both profiles start in a zero-crossing point (from negative to positive ordinates) of their dominant component $H1_0$. A zoom-in detail on first period of Figure 18 is depicted in Figure 19.

Preprints.org (www.preprints.org) | NOT PEER-REVIEWED | Posted: 21 February 2024 doi:10.20944/preprints202402.1238.v1

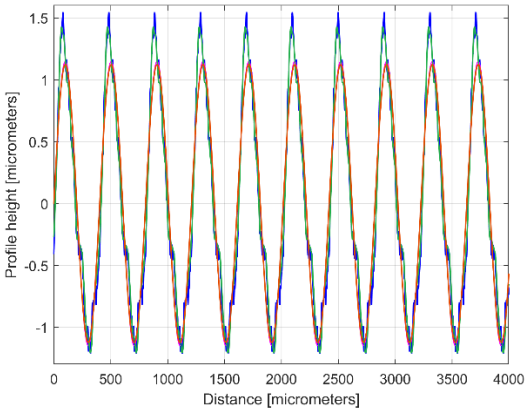

Figure 18. An overlapping of both $y_{dhe0}(x)$ profiles and their dominants $H1_0$.

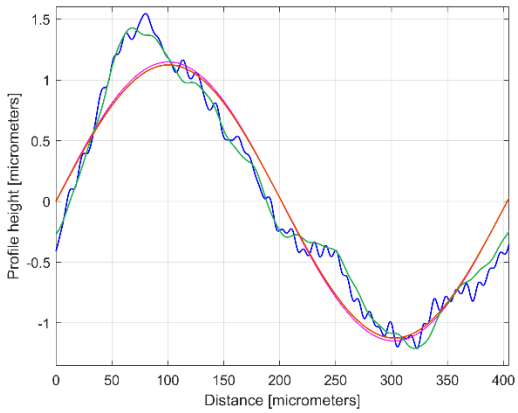

Figure 19. A zoom in detail of Figure 18 with first period of $y_{dhe0}(x)$ profiles and dominants $H1_0$.

As is obvious on Figure 18 and especially in Figure 19, there are strong similarities between the $y_{dhe0}(x)$ profiles (and between dominant components $H1_0$ too). This proves that the proposal of this $y_{dhe0}(x)$ pattern is a useful approach in a comparative analysis of 2DRPs sampled in similar conditions (especially direction) on a flat milled surface with a ball nose end mill.

3.1.1. The Synthesis of a 2D Roughness Profile Pattern on a Period by Profile Averaging

There is another simple option to find out a synthetic (non-analytic) description of a pattern useful to characterize the periodical 2DRPs describable with m conventional periods: the y-coordinate of a point on this pattern (as $y_{ap}(x)$) being an average of the y-coordinates of m points on 2DRP. The distance (measured on x-axis) between each two consecutive points is exactly the conventional period of the dominant H1, as the equivalent wavelength λ_{He1} calculated with $\lambda_{He1}=2\pi/\omega_{He1}$. A y-coordinate value of this average pattern $y_{ap}(x)$ is established by calculus as:

$$y_{ap}(x) = \frac{1}{m}\sum_{i=0}^{m} y(x + i \cdot \lambda_{He1}) \quad \text{with } x = 0 \div \lambda_{He1} \tag{9}$$

The length of this pattern is exactly the conventional period (the wavelength λ_{He1}). A better approach is to describe this $y_{ap}(x)$ pattern starting from the zero-crossing point of the dominant H1 (as $y_{ap0}(x)$, Eq. (10)), this starting point having the x-coordinate $(2\pi-\varphi_{H1})/\omega_{He1}$.

$$y_{ap0}(x) = \frac{1}{m}\sum_{i=0}^{m} y\left(x + \frac{2\pi - \varphi_{H1}}{\omega_{He1}} + i \cdot \lambda_{He1}\right) \quad \text{with } x = 0 \div \lambda_{He1} \tag{10}$$

Here x is the x-coordinate of a generic point on pattern $y_{ap0}(x)$. In Eq. (10), in almost all previous equations (except Eq. (5)) and in the sampled 2DRP, the x-coordinate is numerically described, as x=

Preprints.org (www.preprints.org) | NOT PEER-REVIEWED | Posted: 21 February 2024 doi:10.20944/preprints202402.1238.v1

$l \cdot \Delta x$ for the l^{th} sample, $l=1 \div N$. Here $x+(2\pi-\varphi_{H1})/\omega_{He1}+ i \cdot \lambda_{He1}$ and $x+i \cdot \lambda_{He1}$ in Eq. (9), are also x-coordinates numerically described of samples placed on 2DRP.

Figure 20 presents this $y_{ap0}(x)$ pattern, established by averaging, for the first sampled 2DRP (with $m=9$). It is expected that this averaging (acting as a kind of digital filter) strongly attenuates the non-sinusoidal components (noise) as well as the harmonically uncorrelated ones with the dominant H1. In other words is expected that this $y_{ap0}(x)$ pattern is similar with the first period of $y_{dhe0}(x)$ profile (already depicted in Figure 15). This is fully confirmed in Figure 21, where the $y_{ap0}(x)$ pattern, the $y_{dhe0}(x)$ profile (first period) and the dominant $H1_0$ are overlapped.

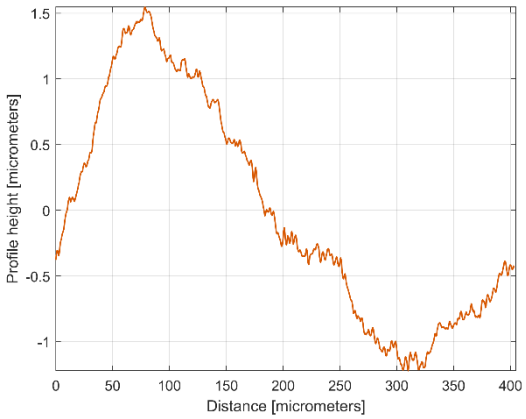

Figure 20. The $y_{ap0}(x)$ pattern of the first 2DRP.

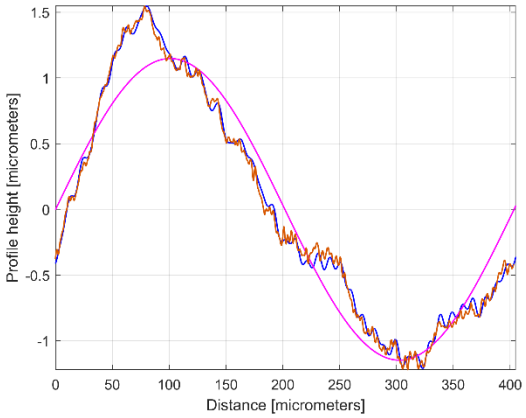

Figure 21. The $y_{ap0}(x)$ pattern of the first 2DRP, overlaid on the first period of $y_{dhe0}(x)$ profile (in blue) and the dominant, $H1_0$.

Similar considerations can be made for the $y_{ap0}(x)$ pattern of the 2nd 2DRP sampled in pick direction, depicted in Figure 22.

There is an interesting utility of these $y_{ap0}(x)$ patterns, similar with the utility of first periods from $y_{dhe0}(x)$ profiles, already stated before in Figure 19: it allows us the synthetic characterization of the roughness profiles, eventually by comparison. As example, Figure 23 depicts a graphical overlapping of the $y_{ap0}(x)$ patterns for both sampled 2DRPs, in pick direction. As expected, there is a very good similarity between $y_{ap0}(x)$ patterns, even better than between $y_{dhe0}(x)$ profiles.

Preprints.org (www.preprints.org) | NOT PEER-REVIEWED | Posted: 21 February 2024 doi:10.20944/preprints202402.1238.v1

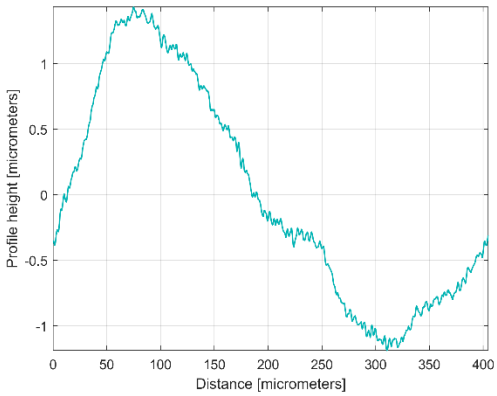

Figure 22. The $y_{ap0}(x)$ pattern of the 2nd 2DRP.

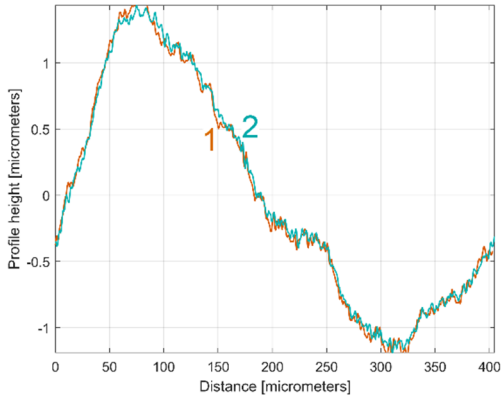

Figure 23. A graphical overlapping of $y_{ap0}(x)$ patterns: 1- for 1st 2DRP; 2 - for 2nd 2DRP.

Certainly, an interesting and easier way to determine a more trustworthy description of a $y_{dhe0}(x)$ profile is the analysis by curve (signal) fitting of the extended $y_{ap0}(x)$ pattern over m successive periods.

3.1.2. An Approach on FFT Spectrum in 2D Roughness Profiles Description

There is another interesting resource that can be exploited related by the mathematical description of $y_{dh}(x)$ profile, particularly $y_{dhe}(x)$ profile. As already stated in Section I, the length of any of two analytical profiles can be artificially increased by mathematical extrapolation (by increasing the number of samples from N to $p \cdot N$), keeping the same sampling rate f_s. This way the conventional frequency resolution (as R_{cfe}) of the FFT spectrum for any of the two extrapolated profiles ($R_{cfe} = f_s/pN$) decreases significantly (by p times compared with the spectra of original profiles having $R_{cf} = f_s/N$ conventional frequency resolution), the Nyquist limit remains unchanged. The quality description of the sinusoidal profile components by means of the FFT spectrum increases significantly.

As a first example, related by first 2DRP, Figure 24 depicts partially (in the 0 ÷ 0.02 μm^{-1} conventional frequency range) the FFT spectrum for $y(x)$ profile (in red, a spectrum already presented before in Figure 5) - and for extrapolated $y_{dhe}(x)$ profile (in blue, with $p = 10$). Figure 25 presents the both spectra on an extended range of conventional frequency (0 ÷ 0.08 μm^{-1}), with the first 27 harmonic correlated sinusoidal components (with $\omega_{Hi} = H_i \cdot \omega_{H1}$).

Preprints.org (www.preprints.org) | NOT PEER-REVIEWED | Posted: 21 February 2024 doi:10.20944/preprints202402.1238.v1

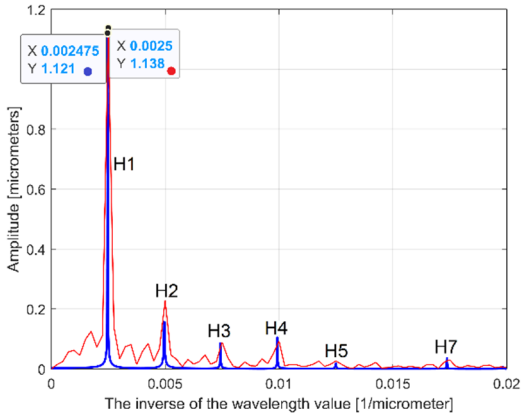

Figure 24. A partial view on the FFT spectra of $y(x)$ profile (in red) and extrapolated $y_{dhe}(x)$ profile with $p=10$ (in blue).

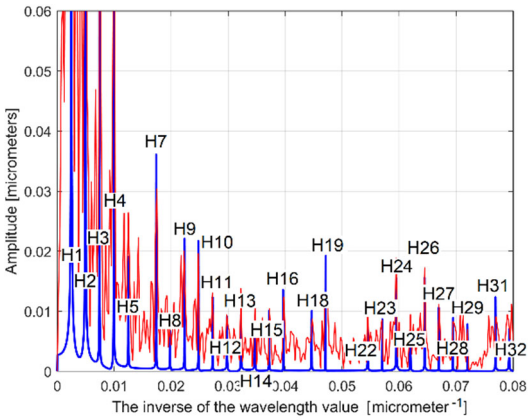

Figure 25. An extended partial view on the FFT spectra of $y(x)$ profile (in red) and extrapolated $y_{dhe}(x)$ profile with $p=10$ (in blue).

Because in this approach the conventional angular frequencies ω_{H1} and ω_{He1} have very similar values (Table 1 and Eq. (5)), the FFT spectrum of extrapolated $y_{dh}(x)$ and $y_{dhe}(x)$ profiles are very similar. The changing of origin of $y_{dhe}(x)$ profile (in order to produce the $y_{dhe0}(x)$ profile) does not produce any change on the FFT spectrum (which is insensitive to phase shifting). The FFT spectrum of extrapolated $y_{dhe}(x)$ and $y_{dhe0}(x)$ profiles are identical.

It is obvious that the FFT spectrum of extrapolated $y_{dhe}(x)$ profile can be used also as a pattern in the comparison of two (or more) 2DRPs, sampled on the same surface, in similar conditions. The similarities between the partial FFT spectra of extrapolated $y_{dhe}(x)$ profiles (with $p=10$) found in both 2DRPs analyzed before, are clearly highlighted in Figure 26, with a zooming on y-axis depicted in Figure 27. For an easier comparison, the FFT spectrum of extrapolated $y_{dhe}(x)$ of 2nd analyzed 2DRP has been artificially moved with 0. 02 μm up and 0.0005 μm^{-1} right.

 doi:10.20944/preprints202402.1238.v1

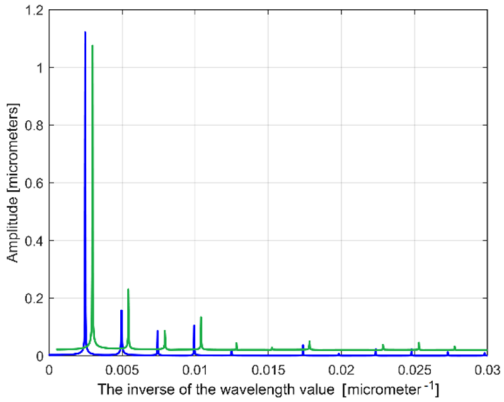

Figure 26. A partial view on the FFT spectra of extrapolated $y_{dhe}(x)$ profiles with $p=10$ (in blue for 1st 2DRP, in green for 2nd 2DRP).

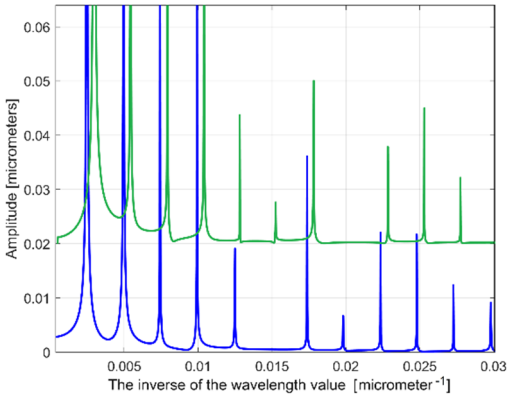

Figure 27. A zoomed image on *y*-axis of the FFT spectra from Figure 26.

In a simpler and trustworthy approach, is possible the investigation of the resources provided by the compared FFT spectra of extended $y_{ap0}(x)$ patterns (related by both 2DRPs) over m successive periods.

3.2. The Analysis of 2D Roughness Profiles in Feed Direction

A similar study is possible on the 2DRPs sampled on the same machined surface, in feed direction, parallel with (d2), in identical conditions, number of samples and sampling rate. It is expected that each of these 2DRPs describe a periodical succession of feed-interval scallops, as traces left by the tips of the milling tool edges during its rotation and feed motion. With a milling tool having three teeth, 5600 rpm rotation speed and 1560 mm/rot feed, the conventional period of these feed-interval scallops should be equal with the feed per tooth $f_t = 0.1$ *mm*.

Figure 28 presents a first 2DRP sampled in feed direction (colored in red), the deterministic part harmonically correlated $y_{dh}(x)$ (as a sum of 11 components, colored in blue) and the residual $r_{11}(x)$ colored in purple. Figure 29 presents the overlapping of the first two periods from the dominant $H1_0$ (curve 1), first two periods of profile $y_{dhe0}(x)$ (curve 2) and the pattern $y_{ap0}(x)$ -with $m = 11$-, extrapolated on two periods (curve 3). As expected, there is a relative good fit between.

 doi:10.20944/preprints202402.1238.v1

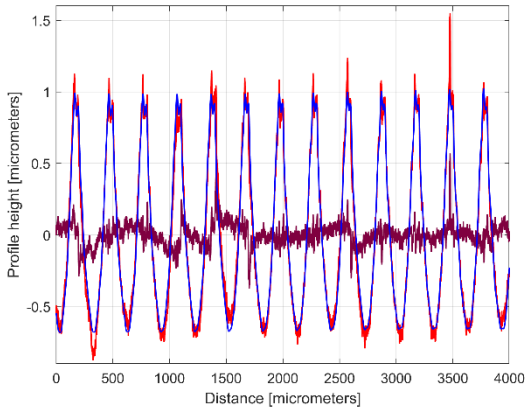

Figure 28. A first 2DRP (in red), the $y_{dh}(x)$ profile (in blue) having 11 components and the 11th residual $r_{11}(x)$ (in purple).

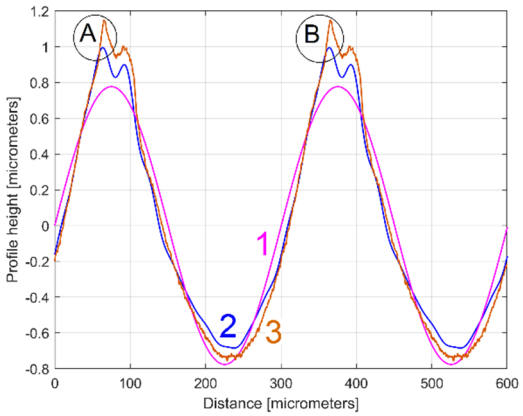

Figure 29. Two conventional periods from: 1 - the dominant component H1$_0$; 2 - the profile $y_{dhe0}(x)$; 3 – the pattern $y_{ap0}(x)$.

Unexpectedly, the conventional angular frequency $\omega_{He1} = 0.020921\ rad/\mu m$ defines the wavelength $\lambda_{He1} = 2\pi/\omega_{He1} = 300.32\ \mu m$, as a conventional period, three times bigger than the feed per tooth ($100\ \mu m$) but practically equal to the feed per milling tool rotation f_r. This means that the 2DRP in feed direction reveals an abnormal behavior of the milling tool, because it rotates off of its axis (with run out, [3]) a single tooth is involved in cutting process. Obviously the theoretical 2DRP in feed direction consists mainly from a group of 2D curve (trochoidal) arcs, as portions of the trajectories of points on the teeth cutting edges. Figure 30 presents a conceptual simulation (without milling tool run out) of these identical trochoidal trajectories (Tr1, Tr2 and Tr3) at high feed rate (for clarity of approach). Figure 31 describes these trajectories with a particularly run out on milling tool: the rotation center is in opposite direction to the point involved in the generation of trajectory Tr2. In both Figures, for down milling, the theoretical 2DRP is described by arcs between the lowest intersection points of trajectories.

Preprints.org (www.preprints.org) | NOT PEER-REVIEWED | Posted: 21 February 2024 doi:10.20944/preprints202402.1238.v1

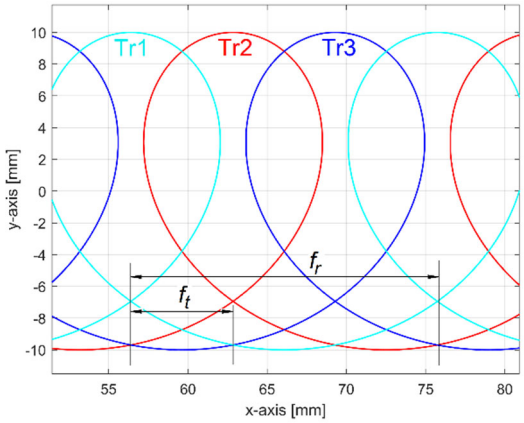

Figure 30. A simulation of 2D trajectories of points placed on teeth cutting edges (no run out).

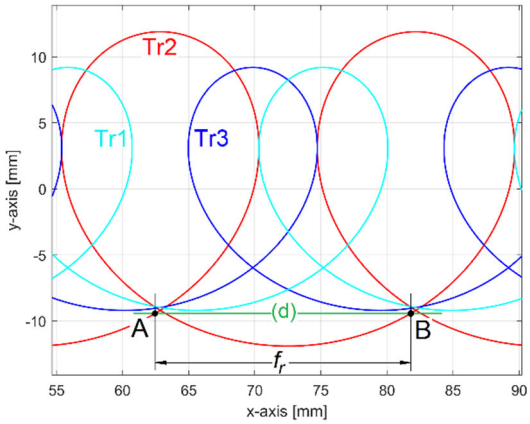

Figure 31. A simulation of 2D trajectories of points placed on teeth cutting edges (with run out).

If the run out is big enough, then the theoretically 2DRP is described by arcs placed on a single trochoidal trajectory, Tr2 on Figure 31. Here (d) is the work piece surface reference line before milling. A conventional period of the dominant component in 2DRP is equal with the feed per rotation (f_r) and not with the feed per tooth ($f_t = f_r/3$). The points A, B from Figure 31 are found in the areas A, B from Figure 29. As opposed to Figure 31, on Figure 29 there is no equality of scales on x and y-axis.

A similar and comparative study can be performed related to a second 2DRP sampled on a straight line (feed direction) as parallel direction to (d2). As opposed to the analysis of 2DRP in pick direction, now this second 2DRP was sampled along a straight line carefully placed as precisely as possible over a whole number of pick-intervals. A correct comparison supposes that the first and second theoretical 2DRP should be the result of the trajectories of the same points on the teeth cutting edges.

The equivalent of Figures 28 is depicted in Figure 32; the equivalent of Figure 29 is depicted in Figure 33. As expected, similarly with Figure 29, there is a relative good fit between the dominant component H1$_0$, $y_{dhe0}(x)$ profile and the pattern $y_{ap0}(x)$.

 doi:10.20944/preprints202402.1238.v1

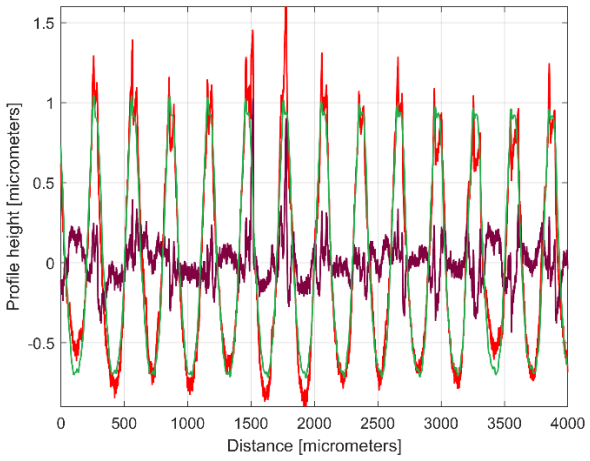

Figure 32. A second 2DRP (in red), the $y_{dh}(x)$ profile (in green) having 11 components and the 11th residual $r_{11}(x)$, (in purple).

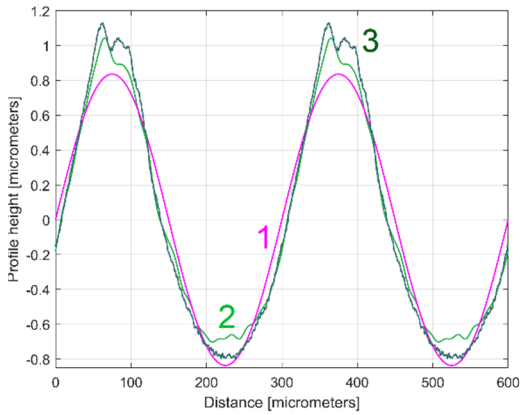

Figure 33. Two conventional periods from: 1 - the dominant component H1$_0$; 2 - the profile $y_{dhe0}(x)$; 3 – the pattern $y_{ap0}(x)$.

As already stated before, related by first 2DRP in feed direction, the same abnormal behavior of the milling tool persists, because the run out, a single tooth is involved in cutting process, the conventional angular frequency being $\omega_{He1} = 0.020946\ rad/\mu m$ defines the wavelength $\lambda_{He1} = 2\pi/\omega_{He1} = 299.97\ \mu m$, as a conventional period or feed per rotation f_r as well (very close on that determined for first profile), three times bigger than the feed per tooth ($100\ \mu m$).

A comparison between Figures 29 and 33 indicates that, similarly with the study in pick direction, there are also strong similarities between these two different 2DRPs sampled in feed direction. Figure 34 depicts the overlapped profiles $y_{dhe0}(x)$, Figure 35 depicts the overlapped of extended patterns $y_{ap0}(x)$, with two periods.

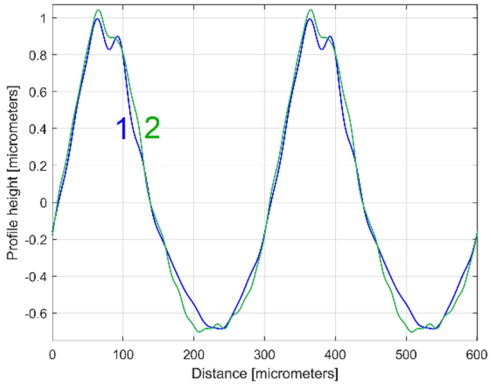

 doi:10.20944/preprints202402.1238.v1

Figure 34. An overlapping of $y_{dhe0}(x)$ profiles for 1st and 2nd 2DRP (1 and 2).

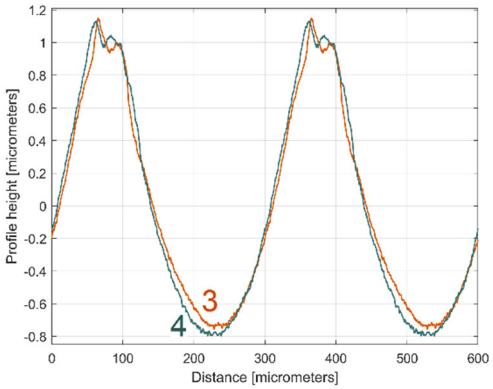

Figure 35. An overlapping of $y_{ap0}(x)$ patterns (two periods) for 1st and 2nd 2DRP (3 and 4).

However we should mention that the coincidence of these two $y_{dhe0}(x)$ profiles (Figure 34) is less good than in the case of the $y_{dhe0}(x)$ profiles for 2DRPs sampled in pick direction (Figure 19). A similarly conclusion is available for the coincidence of $y_{ap0}(x)$ patterns (by comparison between Figures 35 and 23). The main reason for these misfits is the lack of certainty that the two analyzed 2DRPs were generated by the same points of the tool edges.

It is possible also to perform a comparison between the FFT spectra of extrapolated $y_{dh}(x)$ profiles of both 2DRPs, with $p = 10$, as Figure 36 indicates, with zooming on y-axis depicted in Figure 37. For an easier comparison, the FFT spectrum of extrapolated $y_{dh}(x)$ of 2nd analyzed 2DRP has been artificially moved with 0. 01 μm up and 0.0005 μm^{-1} right.

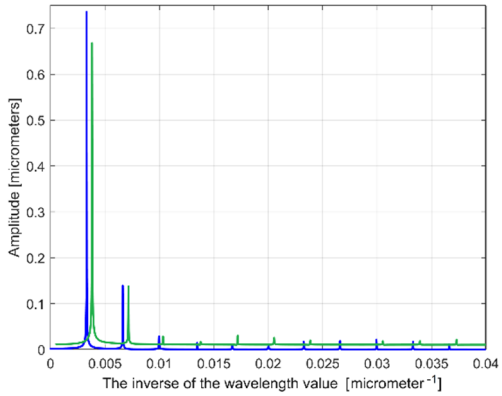

Figure 36. A partial view on the FFT spectra of extrapolated $y_{dhe}(x)$ profiles with $p=10$ (in blue for first 2DRP, in green for second 2DRP).

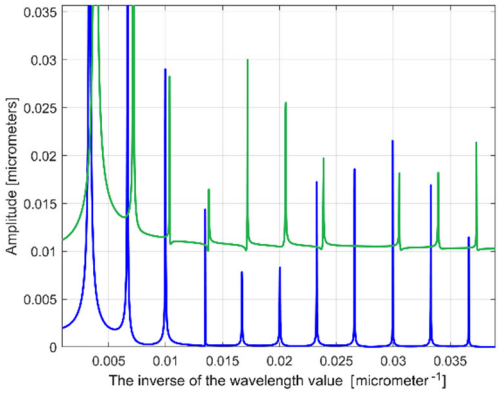

Figure 37. A zoomed image on y-axis of the FFT spectra from Figure 36.

 doi:10.20944/preprints202402.1238.v1

The similarities between spectra of extrapolated $y_{dhe}(x)$ profiles are certain related by conventional frequencies of peaks but less evident related by the peaks amplitudes.

4. Conclusions

The proposed method to analyze and to find (by curve/signal fitting) the mathematical description of the periodical part of an experimental 2D roughness profile, 2DRP (as a sum of sinusoidal components harmonically correlated), provides reliable results, experimentally confirmed, useful to characterize the milled surface (as a sum of wavinesses on two perpendicular directions) and the interaction between the tool and work piece during the milling process (particularly of machined flat surfaces with ball nose end mill, constant step over).

This work proposes an analytical definition of a periodic profile, as a best systematically characterization (pattern) of an experimental 2DRP, sampled with a contact profilometer (in pick and feed directions). A very similar periodic profile (however without an analytical description) is generated using a special kind of sample averaging inside the experimental 2DRP. These periodic profiles are useful for comparison purposes between different experimental 2DRPs or to validate a predictive model for 2DRP [10, 24 and 25] or to achieve the mathematical description of the microgeometry of a milled surface. The shape of these periodic profiles can provide important clues related to the discovery and description of some abnormalities in the milling process (e. g. the tool run out, revealed in this work).

This work proves that the mathematical extrapolation of the analytical defined periodic profile of 2DRP improves the availability of a known but underutilized method of roughness analyzes based on the spectrum of the periodic profile (seen as a time-dependent signal) generated by fast Fourier transform (FFT), with a low (conventional) frequency resolution.

Of course, a generalization of these results in the analysis of other types of milled surfaces (eventually using other roughness sampling methods) is a fully feasible option.

As a future approach, we intend to extend this study to the investigation of the 3D mathematical description of the roughness microgeometry of the complex milled surfaces, experimentally sampled with an appropriate optical system.

Author Contributions: Conceptualization, M.H. and F.C.; methodology, M.H., E.P, C.-G.D. and A.M; software M.H and C.-G.D.; validation F.C, E.P. and A.M; investigation E.P, M.H and D.-F.C.; resources C.-G.D. and D.-F.C.; data curation, M.H., E.P., C.-G.D., A.M. and D.-F.C.; writing—original draft preparation, M.H., F.C, C.-G.D. and A.M; writing-review and editing, E.P. and D.-F.C.; supervision and project administration, M.H. and. C.-G.D.; funding acquisition, C.-G.D. All authors have read and agreed to the published version of the manuscript.

Funding: This research received no external funding.

Data Availability Statement: The data presented in this paper are available upon request addressed to corresponding author.

Acknowledgments: Many thanks to Mitutoyo Romania for donation of the roughness measuring equipment. We would like to express many thanks to our colleagues Neculai-Eugen SEGHEDIN and Eugen CARATA who, some time ago, have equipped the department with several modern CNC machines and equipment. Some of these were used in this study. We also thank our colleague Florentin CIOATA for his support and advices.

Conflicts of Interest: The authors declare no conflicts of interest.

References

1. Chen, J. S.; Huang, Y. K.; Chen, M. S., A study of the surface scallop generating mechanism in the ball-end milling process, *Int. J. Mach. Tools Manuf.* 2005, 45, 9, 1077-1084. https://doi.org/10.1016/j.ijmachtools.2004.11.019
2. Costes, J. P., A predictive surface profile model for turning based on spectral analysis. *J. Mater. Process. Technol.* 2013, 213, 1, 94-100. https://doi.org/10.1016/j.jmatprotec.2012.08.009
3. Ren, Z.; Fang, Z.; Kobayashi, G.; Kizaki, T.; Sugita, N.; Nishikawa, T.; Kugo, J.; Nabata, E., Influence of tool eccentricity on surface roughness in gear skiving. *Precis. Eng.* 2020, 63, 170-176. https://doi.org/10.1016/j.precisioneng.2020.02.007

4. Álvarez-Flórez, J.; Buj-Corral, I; Vivancos-Calvet, J., Analysis of roughness, force and vibration signals in ball-end milling processes. *J. Trends Dev. Mach. Assoc. Technol.* 2015, 19, 11, 1-4.
5. Zahaf, M. Z.; Benghersallah, M., Surface roughness and vibration analysis in end milling of annealed and hardened bearing steel. *Measur. Sens.* 2021, 13, 100035. https://doi.org/10.1016/j.measen.2020.100035
6. Bai, J.; Zhao, H.; Zhao, L.;Cao, M.; Duan, D., Modelling of surface roughness and studying of optimal machining position in side milling. *Int. J. Adv. Manuf. Technol.*, 2021, 116, 3651–3662. https://doi.org/10.1007/s00170-021-07463-y
7. Grzesik, W; Brol, S., Wavelet and fractal approach to surface roughness characterization after finish turning of different workpiece materials. *J. Mater. Process. Technol.* 2009, 209, 5, 2522-2531. https://doi.org/10.1016/j.jmatprotec.2008.06.009
8. Drbúl, M.; Martikáň, P.; Bronček, J.; Litvaj, I.; Svobodová J., Analysis of roughness profile on curved surfaces. MATEC Web Conf. 2018, 244, 01024. https://doi.org/10.1051/matecconf/201824401024
9. Krolczyk, G.; Legutko, S., Experimental analysis by measurement of surface roughness variations in turning process of duplex stainless steel. *Metrol. Meas. Syst*, 2014, XXI, 4, 759–770. DOI: 10.2478/mms-2014-0060.
10. Shang, S.; Wang, C.; Liang, X.; Cheung, C.F.; Zheng, P., Surface roughness prediction in ultra-precision milling: an extreme learning machine method with data fusion. *Micromachines* 2023, 14, 2016. https://doi.org/10.3390/mi14112016
11. Wang, N.; Jiang, F.; Zhu, J.; Xu, Y.; Shi, C.; Yan, H.; Gu, C., Experimental study on the grinding of an Fe-Cr-Co permanent magnet alloy under a small cutting depth. *Micromachines* 2022, 13, 1403. https://doi.org/10.3390/mi13091403
12. Li, J.; Xu, W.; Shen, T.; Jin, W.; Wu, C., Evaluating surface roughness of curved surface with circular profile based on arithmetic circular arc fitting. *Aip. Adv.* 2023, 13, 125312. https://doi.org/10.1063/5.0174008
13. Kundrák, J.; Felhő, C.; Nagy, A., Analysis and prediction of roughness of face milled surfaces using CAD model. *Manuf. Technol*. 2022, 22, 5, 555-572. DOI: 10.21062/mft.2022.061
14. Lazkano, X.; Aristimunno, P. X.; Aizpuru, O.; Arrazola, P. J., Roughness maps to determine the optimum process window parameters in face milling. *Int. J. Mech. Sci.* 2022, 221, 107191. https://doi.org/10.1016/j.ijmecsci.2022.107191
15. Palani, S.; Natarajan, U., Prediction of surface roughness in CNC end milling by machine vision system using artificial neural network based on 2D Fourier transform. *Int. J Adv. Manuf. Technol*. 2011, 54, 1033–1042. DOI 10.1007/s00170-010-3018-3
16. Zeng, Q.; Qin, Y.; Chang, W.; Luo, X., Correlating and evaluating the functionality-related properties with surface texture parameters and specific characteristics of machined components. *Int. J. Mech. Sci.* 2018, 149, 62–72. https://doi.org/10.1016/j.ijmecsci.2018.09.044
17. Filtration techniques for surface texture. Available online: https://guide.digitalsurf.com/en/guide-filtration-techniques.html (accessed on 15.02.2024).
18. Josso, B.; Burton, D. R.; Lalor, M. J., Frequency normalised wavelet transform for surface roughness analysis and characterisation. *Wear* 2002, 252, 5–6, 491-500. https://doi.org/10.1016/S0043-1648(02)00006-6
19. Josso, B.; Burton, D. R.; Lalor, M. J., Wavelet strategy for surface roughness analysis and characterisation, *Comput. Method. Appl. M.* 2001, 191, 829-842. https://doi.org/10.1016/S0045-7825(01)00292-4.
20. Wang, X.; Shi, T.; Liao, G.; Zhang, Y.; Hong, Y.; Chen, K., Using wavelet packet transform for surface roughness evaluation and texture extraction. *Sensors* 2017, 17, 933. https://doi.org/10.3390/s17040933
21. Hao, H.; He, D.; Li, Z.; Hu P.; Chen, Y.; Tang K., Efficient cutting path planning for a non-spherical tool based on an iso-scallop height distance field. *Chinese. J. Aeronaut.* 2023, *in press, uncorrected proof*. https://doi.org/10.1016/j.cja.2023.12.005.
22. Horodinca, M.; Bumbu, N.-E.; Chitariu, D.-F.; Munteanu, A.; Dumitras, C.-G.; Negoescu, F.; Mihai, C.-G., On the behaviour of an AC induction motor as sensor for condition monitoring of driven rotary machines. *Sensors* 2023, 23, 488. https://doi.org/10.3390/s23010488
23. Lecture: Sums of sinusoids (of different frequency). Available online: http://www.spec.gmu.edu/~pparis/classes/notes_201/notes_2019_09_12.pdf (accessed on 15.02.2024).
24. Chen, C.-H.; Jeng, S.-Y.; Lin, C.-J. Prediction and analysis of the surface roughness in CNC end milling using neural networks. *Appl. Sci.* 2022, 12, 393. https://doi.org/10.3390/app12010393
25. Peng, Z.; Jiao, L.; Yan, P.; Yuan, M.; Gao, S.; Yi, J. Wang, X., Simulation and experimental study on 3D surface topography in micro-ball-end milling. *Int. J. Adv. Manuf. Technol.* 2018, 96, 1943–1958. https://doi.org/10.1007/s00170-018-1597-6